scientific reports

Check for updates

OPEN

Performance of MRI-based radiomics for prediction of residual disease status in patients with nasopharyngeal carcinoma after radical radiotherapy

Qinqin Wu[1,2], Weiguang Qiang[3], Liang Pan[1], Tingting Cha[1], Qilin Li[4], Yang Gao[2], Kaiyang Qiu[2] & Wei Xing[1]✉

The purpose of this study was to determine if habitat radiomic features extracted from pretherapy multi-sequence MRI predict residual status in patients with Nasopharyngeal Carcinoma (NPC) after radical radiotherapy. The retrospective study enrolled 179 primary NPC patients, divided into training and validation cohorts at a 7:3 ratio. K-means clustering was employed to segment T2WI, CE-T1WI and FSCE-T1WI images, creating habitats within the volume of interest. Identify relevant features that can recognize NPC residuals. In the training cohort, support vector machine (SVM) models were developed utilizing the radiomic features extracted from each habitat and the entire tumor, selecting the most predictive features for each sequence. SVM models were constructed by combining the optimal radiomic features from each sequences with clinical data. Model performance was compared and validated using receiver operating characteristic (ROC) curves, calibration curves and decision curve analysis (DCA), and differences between models were assessed using the DeLong test. The optimal clustering results revealed 4 habitats in FSCE-T1WI, while 2 habitats in both CE-T1WI and T2WI sequences. In the training cohort, we compared the predictive accuracy of SVM models based on different habitats and total tumor characteristics from three sequences, and found that the features from T2 Hab2, CE-T1 Hab1, and FSCE-T1 Hab4 images showed higher performance. Incorporation of habitat-based radiomic features and clinical variables significantly enhanced the predictive performance. The integrated model exhibits the optimal predictive performance, with the area under the curve (AUC) values of 0.921 (SEN = 0.821, SPE = 0.830) in the training cohort and 0.811 (SEN = 0.778, SPE = 0.722) in the validation cohort. Compared to conventional radiomics, habitat imaging features that distinguish intratumoral heterogeneity have higher predictive value, making them potential non-invasive biomarkers for assessing NPC residual after radiotherapy. Integration of multi-sequence MRI habitat radiomic with clinical parameters further improved predictive accuracy.

Keywords Nasopharyngeal carcinoma, MRI, Habitat radiomics, Post-treatment residual disease, Radiotherapy

Nasopharyngeal carcinoma (NPC) originating from the mucosal epithelium of the nasopharynx is a distinct head and neck tumor with high regional specificity[1]. Epidemiological data indicate that approximately 80% of NPC cases occur in Southern China and Southeast Asia, with an incidence rate of 25–40 per 100,000, making it one of the most common malignancies in these regions[2,3]. Compared to conventional radiotherapy, intensity-modulated radiotherapy (IMRT) has achieved improvements in local control and survival rates, yet 10%~20% of patients still experience local failures[4,5]. Due to tumor heterogeneity, different regions of NPC respond variably

[1]Department of Radiology, The Third Affiliated Hospital of Soochow University, Changzhou First People's Hospital, Changzhou 213003, Jiangsu, China. [2]Department of Radiology, Changzhou Xinbei District Sanjing People's Hospital, Changzhou 213200, Jiangsu, China. [3]Department of Oncology, The Third Affiliated Hospital of Soochow University, Changzhou First People's Hospital, Changzhou 213003, Jiangsu, China. [4]Department of Radiotherapy, The Third Affiliated Hospital of Soochow University, Changzhou First People's Hospital, Changzhou 213003, Jiangsu, China. ✉email: suzhxingwei@suda.edu.cn

to radiation, resulting in residual disease in some patients, which severely impacts their prognosis and outcomes. Post-treatment residuals are a major factor influencing local recurrence and distant metastasis in NPC[6]. According to previous studies[7], timely and accurate identification of patients with residual NPC is crucial for early initiation of salvage radiotherapy or surgical resection, which can improve patient prognosis and survival benefits. Delays in salvage treatment can result in poorer prognoses, underscoring the importance for predictive identification of residual NPC before treatment and the need for tailored, individualized treatment strategies to enhance local control and patient survival rates.

Radiomics technology converts traditional medical images into a set of high-dimensional, quantitative features that provide objective and accurate quantification of tumor phenotypes, and this technology brings great application potential for non-invasive personalized medical care[8]. Some studies have demonstrated that radiomic features can improve prognostic accuracy in NPC patients and offer valuable decision support for future clinical management[9–11]. However, conventional radiomics typically assume tumor homogeneity, focusing solely on radiomics features of the entire tumor while neglecting the heterogeneity between different subregions of the tumor[7,12]. Tumor heterogeneity is pivotal in driving tumor progression, treatment resistance, and disease recurrence. NPC, as an Epstein-Barr virus (EBV)-associated malignancy, is considered a highly genetically heterogeneous disease[13]. A few studies have demonstrated that integrating spatial details of tumors can further enhance the accuracy of disease prognosis prediction[14]. In recent years, in order to analyze tumor heterogeneity more effectively, some researchers have attempted to cluster similar voxels in multi-parameter image data to divide tumors into different sub-regions[15,16]. This method, known as "Habitat Imaging"[17,18], has shown higher potential in distinguishing tumor heterogeneity[19] and has proven prognostic value in breast cancer, hepatocellular carcinoma, and NPC[14]. To our knowledge, no studies have been conducted to date using magnetic resonance imaging (MRI) images for subregional radiomic analysis of post-treatment residues in NPC. This research seeks to ascertain whether radiomic features from habitats better predict post-treatment residuals than the conventional radiomics. Additionally, integrating multidimensional omics data may improve treatment evaluation accuracy given the complexity of NPC.

Results

Clinical characteristics

The characteristics of NPC patients in the two cohorts exhibited a consistent demographic distribution, as summarized in Table 1. A total of 179 eligible patients were included in this study. The mean ages were 51.48 ± 10.63 years and 50.35 ± 9.77 years for the training and validation groups, respectively. Following the 8th edition of AJCC staging, there were 10 cases in stage II, 80 in stage III, and 89 in stage IVa. The numbers of cases for WHO pathological stages I, II and III were 7,18, and 154, respectively. Post-treatment residual disease was identified in 24.8% of patients in the training group and 22.2% in the validation group. Differences in patient sex, age, TNM classification, EGFR status, pathological type, radiotherapy dose, and chemotherapy mode between the training and validation cohorts were well balanced (all $p > 0.05$).

Establishment of intratumoral habitats

Using the GMM and BIC, the optimal number of clusters was identified as 2 for T2WI and CE-T1, and 4 for FSCE-T1. The clustering results were then applied to the original imaging data, producing images that represent distinct habitats. Figure 1 showed the intratumoral segmentation results for a patient with NPC on FSCE-T1,T2WI and CE-T1 MRI.

Radiomics feature extraction and feature selection

Radiomic features from the total tumor and segmented habitats in FSCE-T1, CE-T1, and T2WI MRI were extracted, totaling 1133 features per region. For simplicity, these were named as follows: FSCE-T1 Hab1 (FSCE-T1 Habitat-1), FSCE-T1 Hab2, FSCE-T1 Hab3, FSCE-T1 Hab4, FSCE-T1 total; CE-T1 Hab1, CE-T1 Hab2, CE-T1 total; T2 Hab1, T2 Hab2 and T2 total. Using t-tests or U test, features with $p < 0.05$ were chosen, resulting in 132, 298, 152, 472, 225, 552, 55, 163, 246, 45, 57 and 206 features for FSCE-T1 Hab1-4, FSCE-T1 total, CE-T1 Hab1-2, CE-T1 total, T2 Hab1-2 and T2 total, respectively. These were further filtered using Pearson correlation coefficients, reducing the feature counts to 29, 74, 41, 67, 93, 23, 24, 53, 15, 22 and 47, respectively. Finally, the LASSO method was utilized to choose the remaining radiomic features in the training cohort for model construction, resulting in 13, 7, 10, 12, 16, 13, 11, 14, 4, 8 and 2 optimal radiomic features for the respective regions. The feature selection process in the LASSO method was shown in Fig. 2. The detailed screening information of the habitat features was provided in Supplementary Fig. S1-3. The corresponding coefficient in LASSO for each selected feature were summarized in Supplementary Table S1. Using the coefficients of each radiomic feature in the LASSO method, the habitat radiomics score can be calculated.

Evaluation of radiomic performance based on habitat imaging

We developed SVM models using the most significant radiomic features obtained from the habitats and the entire tumor of FSCE-T1, CE-T1, and T2WI MRI. The predictive effectiveness of all model were presented in Supplementary Table S2. Supplementary Fig. S4 displayed the ROC curves of the SVM models, showing that the high-intensity subregions in FSCE-T1 Hab4, CE-T1 Hab1, and T2 Hab2 demonstrate better predictive performance than the conventional radiomics models (the whole-tumor models) for the corresponding sequences. The AUC values are 0.898 (SEN = 0.868, SPE = 0.875), 0.941 (SEN = 0.892, SPE = 0.882), and 0.876 (SEN = 0.756, SPE = 0.846), respectively. The Delong test indicated notable distinctions between the FSCE-T1 Hab4 and the conventional radiomics models in both the training and validation cohorts. Moreover, notable differences were observed in the training group between all FSCE-T1 subregions and the corresponding conventional radiomics model, as well as between CE-T1 Hab1, T2 Hab2, and their respective conventional

Characteristic	Training cohort ($n=125$)	Validation cohort ($n=54$)	p-value
Age (Years)			0.942
≥ 60	51	21	
< 60	74	33	
Gender			0.370
Male	90	35	
Female	35	19	
Pathologic Classification			0.192
Type I	5	2	
Type II	12	6	
Type III	108	46	
T Stage			0.204
T1	10	3	
T2	17	12	
T3	62	19	
T4a	36	20	
N Stage			0.202
N0	3	5	
N1	27	11	
N2	63	28	
N3	32	10	
Clinical stages			0.803
II	7	3	
III	56	24	
IVa	62	27	
WBC (10^{12}/L)			0.142
Mean (SD)	6.77	5.91	
Median [Min, Max]	6.00 [2.02, 21.13]	4.95 [2.14, 29.92]	
RBC (10^{12}/L)			0.998
Mean (SD)	4.42	4.42	
Median [Min, Max]	4.46 [3.00, 5.58]	4.24 [3.01, 8.71]	
PLT (10^{9}/L)			0.891
Mean (SD)	185.73	176.70	
Median [Min, Max]	176 [72, 498]	168.50 [63, 347]	
NE (10^{9}/L)			0.239
Mean (SD)	5.05	4.40	
Median [Min, Max]	4.18 [0.95, 19.42]	3.77 [1.52, 27.13]	
LMR			0.603
Mean (SD)	12.15	14.17	
Median [Min, Max]	7.56 [0.6, 105.5]	6.45 [0.847, 109.1]	
NLR			0.078
Mean (SD)	4.92	4.05	
Median [Min, Max]	4.17 [0.55, 17.49]	3.10 [0.96, 12.88]	
PLR			0.696
Mean (SD)	0.03	0.03	
Median [Min, Max]	0.02 [0.04, 0.12]	0.02 [0.01, 0.16]	
SII			0.101
Mean (SD)	918.64	728.18	
Median [Min, Max]	654 [85.22, 4477.75]	536.70 [135.32, 3137.91]	
EGFR			0.709
Negative	61	24	
Positive	64	30	
EBER			0.521
Negative	40	19	
Positive	85	35	
Targeted Therapy			0.685

Continued

Characteristic	Training cohort ($n=125$)	Validation cohort ($n=54$)	p-value
No	73	34	
Yes	52	20	
Inducing Chemotherapy			0.614
No	14	4	
Yes	111	50	
Concurrent Chemotherapy			0.983
No	57	24	
Yes	68	30	
GTVnx			0.524
Mean (SD)	70.32	70.17	
Median [Min, Max]	70.32 [59.75, 74.08]	70.26 [64.99, 72.27]	
GTV70			0.682
Mean (SD)	70.11	70.03	
Median [Min, Max]	70.26 [57.89, 73.00]	70.20 [66.22, 72.04]	
Post-Treatment Evaluation			0.758
Residual	31	12	
Non-Residual	94	42	

Table 1. Characteristics of patients with NPC in the training and validation cohorts. NE, neutrophil; LYM, lymphocytes; SII, systemic immune-infammation; PLR, Platelet-to-Lymphocyte ratio; NLR, Neutrophil-to-Lymphocyte ratio; LMR, Lymphocyte-to-Monocyte ratio; GTVnx gross, tumor volume of the nasopharynx; GTV70, gross tumor volume receiving 70 gy.

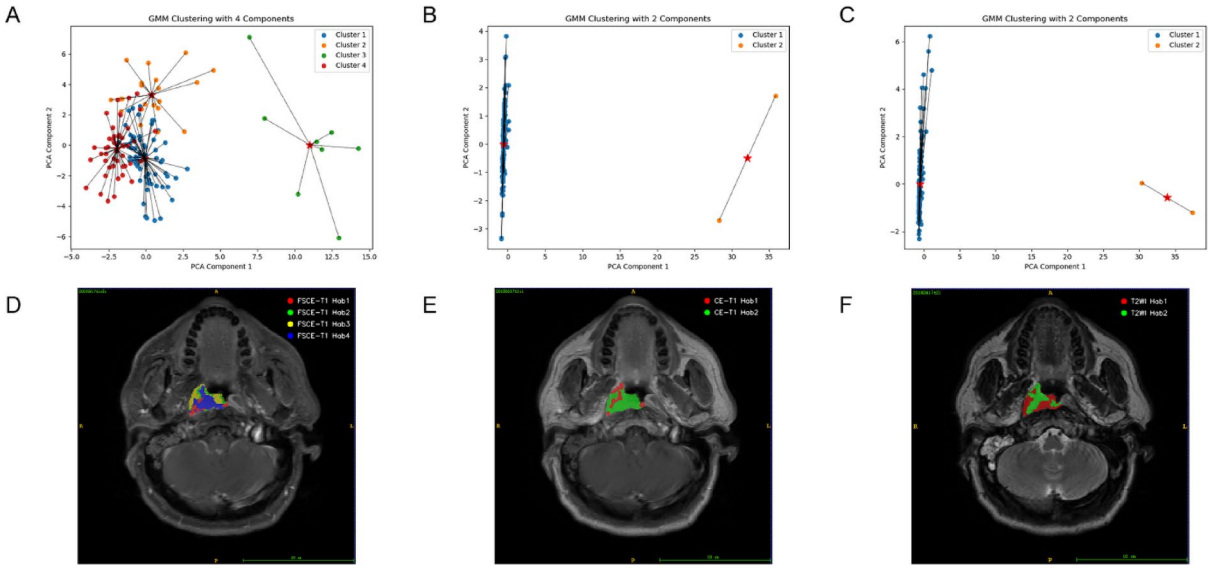

Fig. 1. The optimal cluster number of FS CE-T1 was 4 (**A**), and the optimal cluster number of CE-T1 and T2WI was 2 (**B,C**). The ROI of one patient was grouped into different habitats on FS CE-T1 (**D**), CE-T1 (**E**), and T2WI (**F**), respectively. The red regions correspond to Hab1, green to Hab2, yellow to Hab3, and blue to Hab4.

radiomics models. We compared the predictive accuracy of SVM models based on different habitats and the conventional radiomics from three sequences in the training set, and found that the features from FSCE-T1 Hab4, CE-T1 Hab1, and T2 Hab2 showed higher performance.

The fusion model based on machine learning outperforms traditional clinical predictors

Univariate logistic regression analysis (Table 2) uncovered key factors for detecting residual NPC: Sex, advanced T classification (T4a), advanced clinical stage (IVa), PLT, NE, LYM, NLR, SII, EGFR, and GTVnx ($P<0.05$). Multivariate analysis showed that advanced T classification ($P=0.02$), advanced clinical stage ($P=0.03$), NE

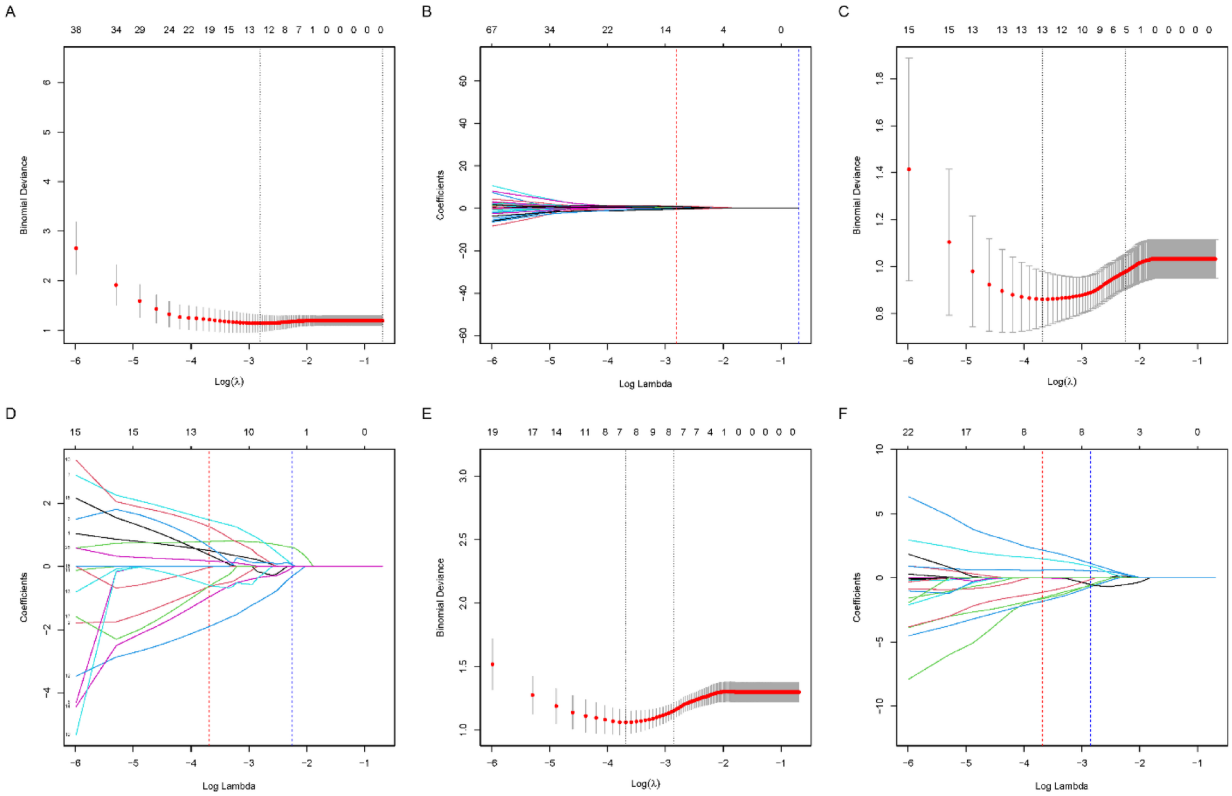

Fig. 2. The variation of partial likelihood deviance in response to changes in lambda during the cross-validation process. The dashed line on the left showed the optimal lambda in the LASSO method with the least partial likelihood deviance (**A-C**). The change of each feature's coefficients in the LASSO method as lambda changes (**D-F**). FS CE-T1 (**A,D**), CE-T1 (**B,E**), and T2WI (**C,F**), respectively.

($P=0.03$), LYM ($P=0.001$), SII ($P=0.01$), and GTVnx ($P=0.008$) were independent predictors of residual disease in NPC.

Integrating these clinical factors with the best habitat-specific Rad-Score from the three sequences, we established five models: Model 1: Clinic, Model 2: Clinic + FSCE-T1 Hab4, Model 3: Clinic + CE-T1 Hab1, Model 4: Clinic + T2 Hab2, Model 5: Clinic + FSCE-T1 Hab4 + CE-T1 Hab1 + T2 Hab2. Table 3 summarized the predictive efficiency of these models. The ROC curves for different models in the training and validation cohorts are illustrated in Fig. 3A, D. The results indicate that the combined model (Model 5) exhibits the best predictive performance, with AUC values of 0.921 (SEN = 0.821, SPE = 0.830) in the training cohort and 0.811 (SEN = 0.778, SPE = 0.722) in the validation cohort. Figure 3B, E showed the DCA in the training and validation cohorts, illustrating that the SVM model with combined habitat-based radiomic scores yields a significant net benefit. Figure 3C, F (the calibration plot) demonstrated the agreement between the model-predicted risk and the observed residue risk, showing that the likelihood of NPC residue was well-calibrated in both the training and validation groups.

Discussion

As artificial intelligence advances rapidly, radiomics-related studies have increasingly provided quantitative and objective support for clinical detection and therapeutic decision-making. Radiomics has shown significant efficacy in various clinical tasks related to NPC[20]. Based on MRI radiomics, numerous studies have shown high value in the diagnosis and differential diagnosis[21,22], staging[23], treatment efficacy[24,25], prediction of treatment side effects[26,27], and prognosis[28,29] of NPC. However, few studies have reported on the use of radiomics to predict residual disease post-treatment in NPC. Residual NPC is a major factor influencing local recurrence and distant metastasis[7]. Within the framework of modern precision medicine, early identification of residual NPC enables tailored interventions and treatment adjustments, improving local control and patient survival.

Conventional radiomics studies mainly focus on the overall primary tumor of NPC, often neglecting intratumoral heterogeneity.Heterogeneity within the tumor suggests that the spatial distribution of NPC is uneven, which may manifest differently at the micro-scale voxel level. In contrast to conventional approaches, we adopted a habitat technique[30] in our research, a novel method that clusters solid tumors in pre-treatment images and then extracts radiomic features from resulting subregions. This approach helps to exclude regions unrelated to post-treatment residual NPC during feature extraction, thus improving the model's predictive accuracy. Habitat imaging, as a subregion radiomics analysis technique, allows for the measurement of tumor subregions that are closely associated with tumor growth and invasiveness[16]. Xu et al.[11] utilized PET/CT to

Characteristics	Univariate logistic regression		Multivariate logistics regression	
	OR (95%CI)	*P* value	OR (95%CI)	*P* value
Sex	2.87 (1.39 ~ 5.89)	**0.0001**	1.88 (0.64 ~ 5.47)	0.25
Age	1.13 (0.61 ~ 2.06)	0.70		
Pathologic Classification				
Type I	Reference			
Type II	0.85 (0.14 ~ 4.99)	0.86		
Type III	0.95 (0.21 ~ 4.38)	0.95		
T Stage				
T1	Reference			
T2	2.50 (0.26 ~ 23.87)	0.43		
T3	4.76 (0.58 ~ 38.72)	0.95		
T4a	49.09 (5.75 ~ 418.88)	< **0.0001**	20.56 (2.13 ~ 514.66)	**0.02**
N Stage				
N0	Reference			
N1	0.52 (0.11 ~ 2.42)	0.41		
N2	0.65 (0.15 ~ 2.79)	0.57		
N3	1.00 (0.22 ~ 4.54)	1.00		
Clinical stages				
II	Reference			
III	2.08 (0.24 ~ 17.67)	0.50		
IVa	16.84 (2.04 ~ 139.08)	**0.01**	1.41 (0.15 ~ 32.30)	**0.03**
WBC	1.12 (1.0 ~ 1.25)	0.05		
RBC	0.78 (0.45 ~ 1.34)	0.37		
PLT	1.01 (1.0-1.01)	**0.02**	1.0 (0.10 ~ 1.01)	0.29
NE	1.17 (1.03 ~ 1.32)	**0.01**	1.28 (1.03 ~ 1.62)	**0.03**
LYM	0.27 (0.13 ~ 0.57)	**0.0001**	0.004 (0 ~ 0.07)	**0.001**
LMR	0.89 (0.49 ~ 1.62)	0.71		
NLR	2.88 (1.55 ~ 5.34)	< **0.0001**	0.49 (0.09 ~ 2.62)	0.42
PLR	0.94 (0.52 ~ 1.71)	0.85		
SII	3.19 (1.59 ~ 6.41)	< **0.0001**	3.51 (1.37 ~ 0.50)	**0.01**
EGFR	2.10 (1.02 ~ 4.32)	**0.04**	1.73 (0.52 ~ 5.74)	0.37
EBER	1.85 (0.97 ~ 3.53)	0.06		
Targeted Therapy	1.24 (0.68 ~ 2.27)	0.49		
Inducing Chemotherapy	0.68 (0.26 ~ 1.80)	0.43		
Concurrent Chemotherapy	1.39 (0.76 ~ 2.53)	0.29		
GTVnx	0.70 (0.52 ~ 0.96)	**0.03**	0.68 (0.50 ~ 0.89)	**0.008**
GTV70	0.90 (0.64 ~ 1.27)	0.54		

Table 2. Univariate and multivariate analyses of risk factors for residual in patients with NPC.

Cohort	Model	AUC (95% CI)	Accuracy	Sensitivity	Specificity	*P* value
Train	Clinic	0.759 (0.727 ~ 0.791)	0.728	0.698	0.828	ref
	Clinic + FSCE-T1 Hab4	0.831 (0.785 ~ 0.876)	0.808	0.793	0.837	**0.030**
	Clinic + CE-T1 Hab1	0.834 (0.783 ~ 0.884)	0.784	0.771	0.810	0.075
	Clinic + T2 Hab2	0.861 (0.812 ~ 0.910)	0.792	0.803	0.776	**0.002**
	Clinic + FSCE-T1 Hab4 + CE-T1 Hab1 + T2 Hab2	0.921 (0.867 ~ 0.975)	0.824	0.821	0.830	< **0.0001**
Test	Clinic	0.659 (0.620 ~ 0.699)	0.828	0.705	0.800	ref
	Clinic + FSCE-T1 Hab4	0.781 (0.711 ~ 0.850)	0.778	0.784	0.765	0.071
	Clinic + CE-T1 Hab1	0.714 (0.642 ~ 0.785)	0.722	0.725	0.714	0.412
	Clinic + T2 Hab2	0.737 (0.664 ~ 0.810)	0.741	0.788	0.667	0.120
	Clinic + FSCE-T1 Hab4 + CE-T1 Hab1 + T2 Hab2	0.811 (0.730 ~ 0.892)	0.759	0.778	0.722	**0.0047**

Table 3. The performance of 5 SVM models for predicting NPC residue. AUC, area under the curve; P values are derived from the DeLong's test of AUCs, where AUC of clinic is the reference standard for comparison.

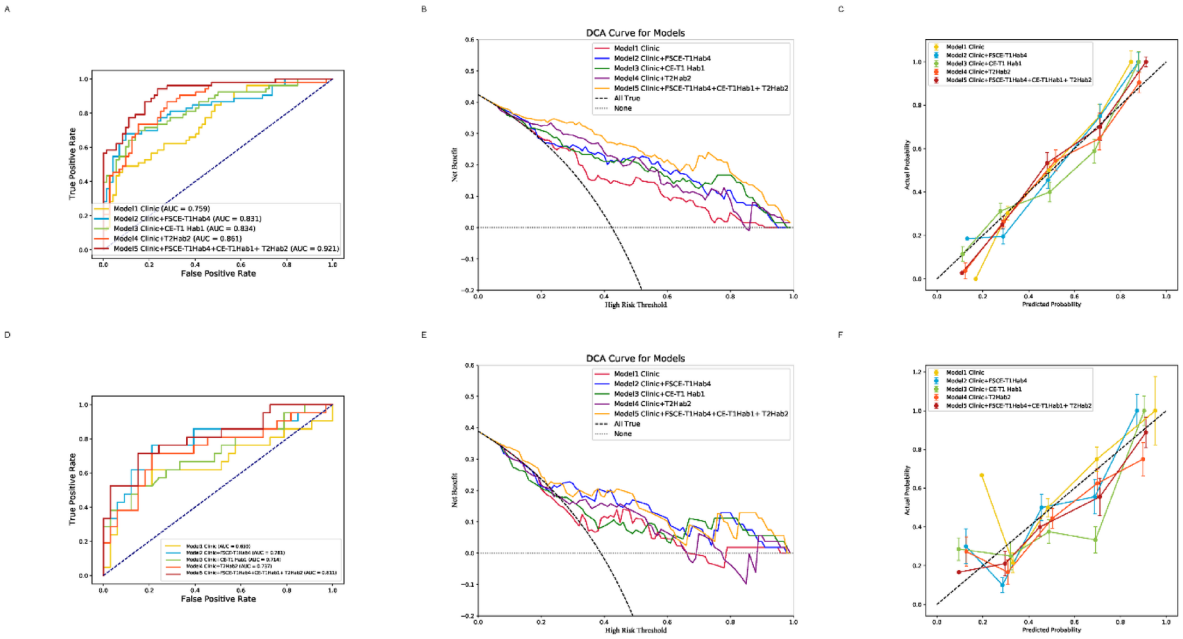

Fig. 3. Based on clinical data and the habitat-specific Rad-Score, we constructed five types of models: Model 1 (Clinic), Model 2 (Clinic + FSCE-T1 Hab4), Model 3 (Clinic + CE-T1 Hab1), Model 4 (Clinic + T2 Hab2), and Model 5 (Clinic + FSCE-T1 Hab4 + CE-T1 Hab1 + T2 Hab2). ROC of the five models to predict residues with NPC in training cohort and test cohort (**A, D**). DCA curves of the models developed in the training and validation cohorts (**B, E**). Calibration curves of the models developed in the training and validation cohorts (**C, F**).

identify significantly heterogeneous habitats in NPC and developed habitat radiomics methods to predict progression-free survival (PFS) in NPC patients.

The sub-regional analysis performed here underscored the crucial role of habitat analysis in detecting residual heterogeneity in NPC post-radiotherapy. After optimizing the cluster count, we discerned distinct habitats across FSCE-T1, CE-T1, and T2WI MRI sequences using the K-means clustering method. The results showed that information obtained from FSCE-T1 Hab4, CE-T1 Hab1 and T2 Hab2 was more valuable for distinguishing residual NPC post-treatment. This could be due to the capability of habitat radiomics to more accurately capture tumor variability and distinguish features between individuals, especially within the tumor microenvironment. These results are consistent with previous reports, suggesting that habitat models constructed through quantitative analysis of intratumoral heterogeneity possess enhanced predictive capabilities[31]. The discriminatory performance of the models, as indicated by AUC values, was superior for CE-T1 Hab1, FSCE-T1 Hab4 and T2 Hab2 compared to other habitats and the conventional radiomics in the CE-T1, FSCE-T1 and T2WI sequences, respectively. This indicates that, when reliable radiomic features are extracted, voxel feature clustering of subregions derived from MRI may also define tumor interior regions associated with heterogeneity.

Our study also identified that the FSCE-T1 Hab4, CE-T1 Hab1, and T2 Hab2 subregions were spatially mapped to areas of slightly hypointense signal intensity within NPC lesions, which may correspond to regions of low perfusion or densely proliferating tumor cells. Gadolinium diethylenetriamine pentaacetic acid (Gd-DTPA), as a contrast agent, shows gradient-enhanced signals, revealing the tumor's intrinsic biological characteristics. For FSCE-T1 and CE-T1, the intra-tumor habitats characterized by high cellular proliferation density demonstrated higher diagnostic accuracy compared to those with low cellular density and the conventional radiomics (FSCE-T1 Hab4 AUC = 0.898; CE-T1 Hab1 AUC = 0.941). Radiation therapy can inhibit tumor progression by inducing DNA damage through direct ionization or indirectly by stimulating the creation of reactive oxygen species (ROS). The effectiveness of these indirect effects largely depends on the presence of oxygen[32]. T2 Hab2, as a water molecule-dense region, may generate a large number of oxygen free radicals under X-ray irradiation, promoting tumor cell death. The superior predictive information provided by the T2 Hab2 over Hab1 and the entire tumor may represent ischemic and hypoxic conditions, leading to radioresistance and greater heterogeneity compared to other regions. Exploring intratumoral heterogeneity can reveal important clues to the potential mechanisms driving radiotherapy resistance in NPC. We need further studies to confirm this.

Finally, we compared the performance of radiomic score based on the optimal predictive habitat from three MRI sequences with the combination of clinical variables and blood parameters in predicting residual NPC post-treatment. The results showed that integrating the optimal predictive habitats' radiomic score with clinical variables and blood parameters achieved the highest predictive accuracy across both the training and validation sets. This can be explained by the fact that the occurrence and development of NPC itself are extremely complex,

and multi-dimensional information collectively characterizes feature predictions, which can further enhance assessment efficiency.

This investigation is not without its limitations. First, its retrospective design and small cohort size call for larger prospective datasets to improve model performance. Second, the data were obtained from a single center and future efforts should include multi-center data to improve model generalizability. Third, K-means clustering was used to identify optimal habitats from FSCE-T1, CE-T1, and T2WI sequences. Whether more clustering subregions could achieve better performances is worth further investigation. Some studies have demonstrated that combining functional and structural imaging data improves the accuracy of tumor subregion delineation and captures biologically relevant heterogeneity[33–35]. Additionally, spatial transcriptomics enables the mapping of gene expression patterns within tumor subregions[36–38]. Future research could integrate functional imaging and biological data to refine clustering strategies and enhance the biological relevance of tumor habitats[33–35]. Lastly, understanding and labeling the clusters remains challenging, requiring validation with clinical outcomes. The study suggests that habitat imaging segmentation holds promise for capturing greater tumor heterogeneity, but it still requires further computational resources and verification to demonstrate its clinical effectiveness. Additional research is needed to elucidate the relationship linking clinical phenotypes (e.g., hypoxia, treatment resistance) with their radiomic features.

In conclusion, the habitat-based approach outperforms conventional radiomics in predicting post-treatment residuals in NPC, serving as a non-invasive biomarker. Integrating habitat radiomics with clinical and blood parameters enhances the model's ability to identify residual NPC after radiotherapy, aiding in the adjustment of treatment strategies and the implementation of more rational and individualized interventions, ultimately improving local control and patient survival.

Materials and methods

Patients

This work has been approved by the Ethics Committee of Changzhou First People's Hospital (approval NO.2023016) and was conducted in accordance with the Declaration of Helsinki of 1975, revised in 2013. Due to the retrospective nature of the study, the Ethics Committee of Changzhou First People's Hospital waived the need of obtaining informed consent. This research collected data from 219 NPC patients with clinical stages I-IVa, who received radical radiotherapy between January 2015 and December 2019. The inclusion criteria were comprised: (1) pathologically verified newly diagnosed NPC, (2) staging of I-IVa based on the 8th edition of the AJCC TNM staging system, (3) availability of high-quality MRI of the nasopharynx and neck before treatment and three months post-radiotherapy, including transverse T2-weighted imaging (T2WI), contrast-enhanced T1-weighted imaging (CE-T1WI), and fat-suppressed contrast-enhanced T1-weighted imaging (FSCE-T1WI), (4) a minimum follow-up period of 18 months, and complete IMRT treatment. Exclusion criteria included: (1) distant metastasis at initial diagnosis, (2) failure to complete radiotherapy due to severe side effects or personal reasons, (3) prior chemo- or radiotherapy or other anti-tumor treatments, (4) absence of pre-treatment MRI images or poor image quality unsuitable for analysis, (5) concurrent primary malignancies at other sites, (6) patients with severe heart, lung, liver, or kidney diseases. The patient selection and categorization process is depicted in Fig. 4. Based on the above criteria, a total of 179 NPC patients were contained in this work. Patients were allocated to the training group ($n = 125$) and the validation group ($n = 54$) in a ratio of 7:3 using computer-generated random numbers.

All enrolled NPC patients received 0–3 cycles of induction chemotherapy, including either nedaplatin + 5-fluorouracil (TF) or docetaxel + nedaplatin (or cisplatin) + 5-fluorouracil (TPF). Concurrently with radiotherapy, patients underwent 0–2 cycles of chemotherapy with nedaplatin or cisplatin. All patients completed radical IMRT. The prescribed radiation dose for the primary nasopharyngeal gross tumor volume (PGTVnx) ranged from 67.89 to 73 Gy.

Residual disease was defined as the failure of the tumor to completely disappear three months after adequate radiotherapy, confirmed pathologically as residual tumor. In cases where MRI indicated residual disease but lacked pathological confirmation, additional evaluations such as PET/CT, nasopharyngoscopy, follow-up results, and multidisciplinary clinical discussions were used to determine the presence of residual disease. Assessments were performed by one experienced radiation oncologist and two radiation oncologists with over ten years of experience, relying on MRI scans obtained prior to treatment and three months afterward.

MRI acquisition and image preprocessing

All patients underwent routine MRI scans of the head and neck, performed using a Siemens Verio 3.0T superconducting MRI system. Gadopentetate dimeglumine was used as the contrast agent. The routine MRI scans included: (1) axial T1WI with parameters TR 830 ms, TE 13 ms, field of view (FOV) 230 mm × 256 mm, matrix 320 × 224, flip angle 150°, (2) axial T2WI with parameters TR 3500 ms, TE 79 ms, FOV 230 mm × 230 mm, matrix 384 × 288, flip angle 150°, and (3) axial CE-T1WI and FSCE-T1WI utilizing a gadopentetate dimeglumine injection at a dosage of 0.2 ml/kg (parameters TR 550 ms, TE 8.89 ms, FOV 230 mm × 230 mm, matrix 256 × 168, flip angle 90°). All scanning protocols included a slice thickness of 5.0 mm and an interslice interval of 1.0 mm.

MRI images of all enrolled cases were extracted from PACS and preprocessed. First, the N4ITK algorithm was employed to correct bias field artifacts, reducing radiofrequency field inhomogeneity and interference from the MRI equipment. Second, the grayscale values of the images were normalized to the range (0-255) to reduce differences in grayscale between different sequences, acquisition times, and parameter settings, ensuring the accuracy and reliability of texture analysis. Additionally, to account for imaging feature differences due to variations in reconstruction slice thickness and pixel size, images were processed to a uniform size of

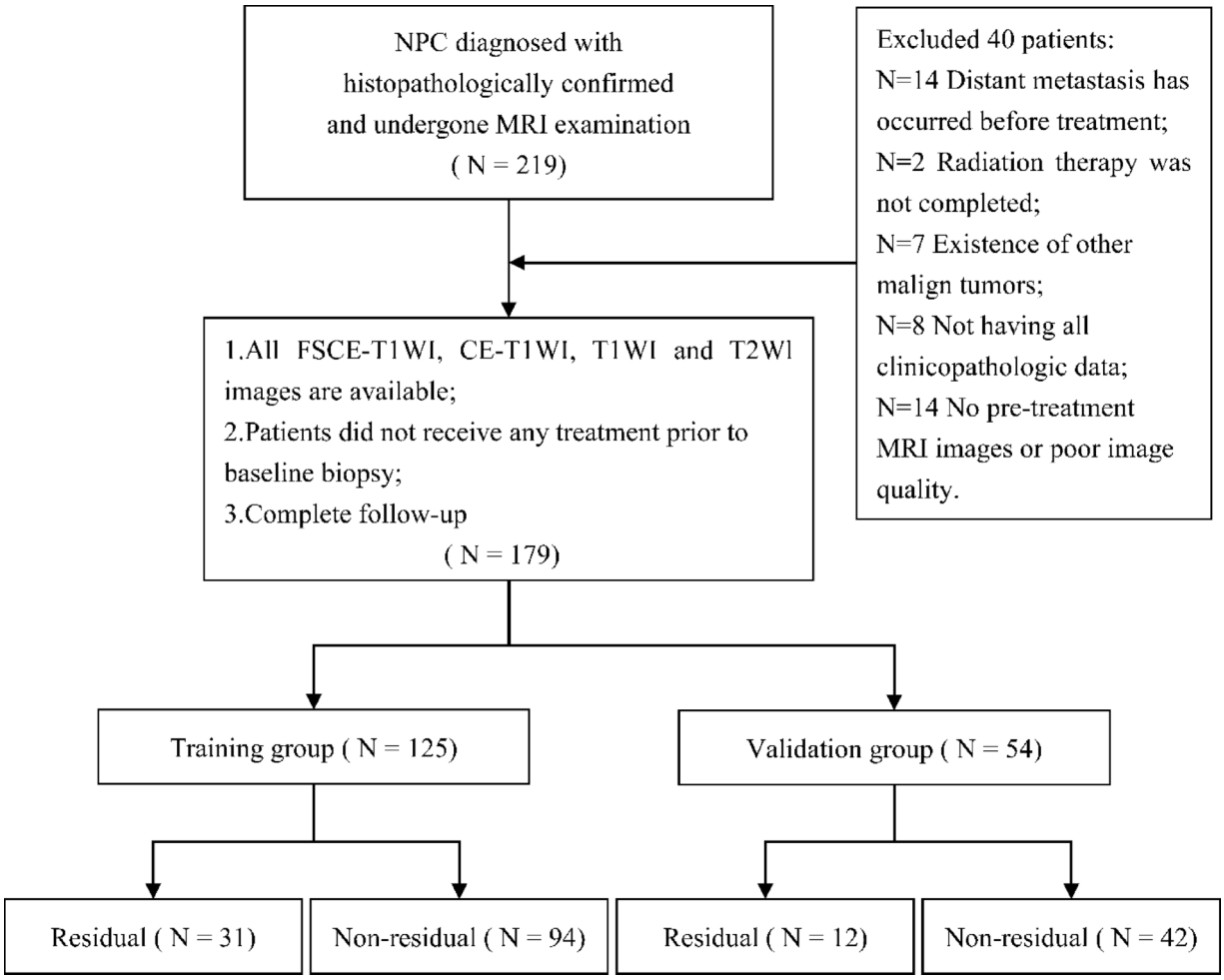

Fig. 4. Flowchart shows patient selection and classification.

$1 \times 1 \times 1$ mm^3. Preprocessing was implemented using Simple ITK 1.2.4, an open-source platform in Python 3.7.0 (www.python.org).

Image segmentation

The study design workflow is depicted in Fig. 5. Image registration of FSCE-T1 and CE-T1 sequences was performed based on the T2WI sequence. We used 3D Slicer version 4.11 (https://www.slicer.org/) for manual image segmentation. On the T2WI sequence, the three-dimensional volume of interest (VOI) was manually delineated slice by slice. The tumor margins were primarily segmented on the T2WI sequence, followed by cross-verification of the precision of tumor margins using the CE-T1 and FSCE-T1WI sequences. For tumors that did not significantly enhance, the tumor margins were segmented slice by slice based on the FSCE-T1WI sequence, and then cross-verified with the aforementioned sequences for precision. The obtained VOIs were applied to the above sequences for multi-sequence VOI extraction. The regions of interest (ROIs) were delineated by two experienced radiation oncologists and subsequently reviewed for intra- and inter-reader concordance by a senior radiation oncologist with 15 years of expertise.

Habitat generation

In our study, to objectively delineate habitats within the tumor, we employed a straight forward linear interaction clustering approach based on magnetic resonance imaging (MRI) data[39]. Using PyRadiomics[40] (https://pyradiomics.readthedocs.io), we extracted a sum of 106 radiomic features from the entire tumor, in accordance with the standards established by the Image Biomarker Standardization Initiative[41]. These features encompassed 18 histogram-based metrics, 14 shape-based metrics, and 74 texture-based metrics. The clustering analysis utilized a Gaussian Mixture Model (GMM) to identify the best number of clusters that reflect the tumor's internal heterogeneity. The Bayesian Information Criterion (BIC) was applied impartially to ascertain the optimal clustering count, ranging from 1 to 8, which effectively captured the tumor's internal heterogeneity[42]. Thereafter, the K-means algorithm was applied to cluster sub-regions for each sample.These clustering results were subsequently applied to the original imaging data to generate images representing distinct habitats.

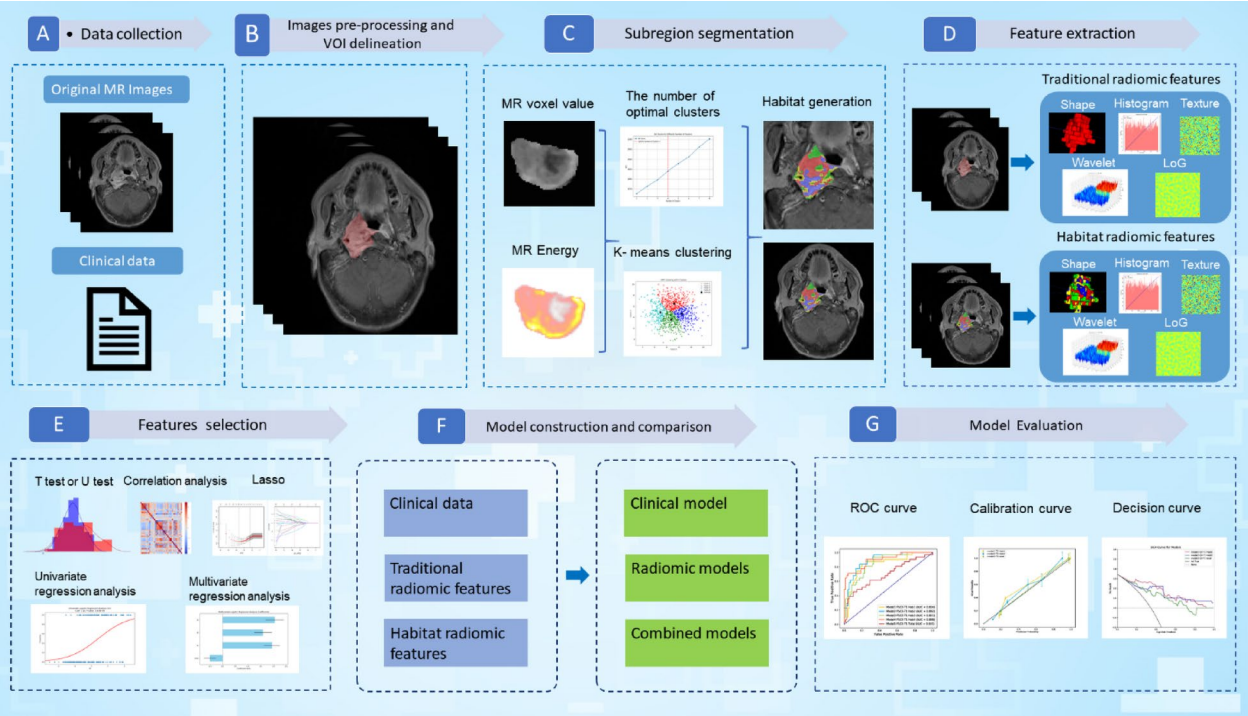

Fig. 5. The workflow of this study. (**A**) Collection of multiparametric MRI images and clinical data. (**B**) Tumor segmentation on the images. (**C**) Generation of subregion label maps using Bayesian Gaussian Mixture Model and K-means clustering algorithms. (**D**) Extraction of conventional radiomic features and habitat radiomic features. (**E**) Selection of residue-related features using a series of feature selection strategies. (**F**) Construction of models and comparison between different models. (**G**) The validation of the models.

Feature extraction

Fifty patients were randomly selected, and lesions were independently delineated by two blinded observers across multiple imaging sequences. Two segmentation masks were generated per sequence, and radiomic features were extracted from both sets. Intra-class correlation coefficients (ICCs) assessed inter-observer reproducibility, with features retaining ICC > 0.75 included for further analysis. Using the PyRadiomics platform with Python (version 3.7.0), we extracted features from each habitat and the entire tumor. For feature extraction, we utilized wavelet and Laplacian of Gaussian (LoG) image filters. The Sigma parameter of the LoG filter defined the texture roughness to be highlighted, with sigma values set at 1, 3, and 5 to generate filtered images with varying textures. In wavelet filtering, the bin width was configured to 25. Consequently, 1133 radiomic features were derived from each habitat and the entire tumor region, comprising: (1) shape features, (2) first-order histogram-based features, (3) texture features, (4) wavelet features and (5) LoG features.

Feature selection

To ensure comparability across different features, we applied Z-score normalization to standardize data to the same scale. Using Students' t test or the Mann-Whitney U test, we selected radiomic features with significant differences ($p < 0.05$). Given the significant redundancy in the original data, a correlation analysis was conducted. Features with absolute correlation coefficients exceeding 0.85 were excluded based on the correlation matrix calculated for the training cohort. Finally, the feature reduction and selection process was carried out using the least absolute shrinkage and selection operator (LASSO). We adapted LASSO regression to establish the radiomic score (Rad-Score). To prevent overfitting, we employed 10-fold cross-validation.

Model development, validation

Using the features selected from each habitat and the entire tumor, we constructed a SVM classification model in the training cohort, which was subsequently verified in the validation cohort. The ROC curve was plotted, and the AUC was used to assess the performance of each model, with the DeLong test comparing AUC values of different models. The optimal model for predicting NPC residuals was identified for each MRI sequence, and the best habitat-specific Rad-Score for each sequence was established for each patient using the most important radiomic features.

To determine independent risk factors for residual NPC, we conducted univariable and multivariable logistic regression analyses on potential predictors from clinical data, including gender, age, pathology type, T stage and so on. These independent risk factors were then combined with the habitat-specific Rad-Score of each MRI sequence to form various composite models. The performance of each model was measured using AUC, with the AUC values of the various models being compared through the DeLong test.

Statistical analysis

All statistical analyses were conducted using SPSS (version 26.0, available at https://www.ibm.com) and R software (version 4.4.0, http://www.rproject.org). To assess whether the quantitative data followed a normal distribution, the Shapiro-Wilk test was employed. When measurement data exhibited a normal distribution, they were presented as mean ± standard deviation (mean ± SD), and the independent samples t-test was employed for comparing groups. For data not conforming to a normal distribution, values were displayed as (interquartile range) [M (P25 and P75)], and comparisons among groups were performed using the Mann-Whitney U test. The $\chi 2$ test was employed to assess differences in categorical variables across groups. Statistical significance was defined as a P value under 0.05.

Data availability

The data cannot be made publicly available upon publication because they contain sensitive personal information. The data that support the findings of this study are available upon reasonable request from the corresponding author.

Received: 9 October 2024; Accepted: 25 April 2025
Published online: 14 May 2025

References

1. Zeng, F., Ye, Z. & Zhou, Q. CT-based peritumoral radiomics nomogram on prediction of response and survival to induction chemotherapy in locoregionally advanced nasopharyngeal carcinoma. *J. Cancer Res. Clin. Oncol.* **150**, 50. https://doi.org/10.1007/s00432-023-05590-5 (2024).
2. Chen, Y. P. et al. Nasopharyngeal carcinoma. *Lancet* **394**, 64–80. https://doi.org/10.1016/S0140-6736(19)30956-0 (2019).
3. Luo, W. Nasopharyngeal carcinoma ecology theory: cancer as multidimensional Spatiotemporal unity of ecology and evolution pathological ecosystem. *Theranostics* **13**, 1607–1631. https://doi.org/10.7150/thno.82690 (2023).
4. Lee, A. W. M. et al. Management of locally recurrent nasopharyngeal carcinoma. *Cancer Treat. Rev.* **79**, 101890. https://doi.org/10.1016/j.ctrv.2019.101890 (2019).
5. You, R. et al. Hyperfractionation compared with standard fractionation in intensity-modulated radiotherapy for patients with locally advanced recurrent nasopharyngeal carcinoma: a multicentre, randomised, open-label, phase 3 trial. *Lancet* **401**, 917–927. https://doi.org/10.1016/S0140-6736(23)00269-6 (2023).
6. Xi, Y. et al. Early prediction of long-term survival of patients with nasopharyngeal carcinoma by multi-parameter MRI radiomics. *Eur. J. Radiol. Open.* **12**, 100543. https://doi.org/10.1016/j.ejro.2023.100543 (2024).
7. Wu, S. et al. Differences in radiomics signatures between patients with early and advanced T-Stage nasopharyngeal carcinoma facilitate prognostication. *J. Magn. Reson. Imaging.* **54**, 854–865. https://doi.org/10.1002/jmri.27633 (2021).
8. Zhong, L. et al. A deep learning-based radiomic nomogram for prognosis and treatment decision in advanced nasopharyngeal carcinoma: A multicentre study. *EBioMedicine* **70**, 103522. https://doi.org/10.1016/j.ebiom.2021.103522 (2021).
9. Fang, M. et al. Multi-Habitat based radiomics for the prediction of treatment response to concurrent chemotherapy and radiation therapy in locally advanced cervical Cancer. *Front. Oncol.* **10**, 563. https://doi.org/10.3389/fonc.2020.00563 (2020).
10. Wu, M. et al. MRI-based clinical radiomics nomogram May predict the early response after concurrent chemoradiotherapy in locally advanced nasopharyngeal carcinoma. *Front. Oncol.* **13**, 1192953. https://doi.org/10.3389/fonc.2023.1192953 (2023).
11. Xu, H. et al. Subregional radiomics analysis of PET/CT imaging with intratumor partitioning: application to prognosis for nasopharyngeal carcinoma. *Mol. Imaging Biol.* **22**, 1414–1426. https://doi.org/10.1007/s11307-019-01439-x (2020).
12. Ouyang, F. S. et al. Exploration and validation of radiomics signature as an independent prognostic biomarker in stage III-IVb nasopharyngeal carcinoma. *Oncotarget* **8**, 74869–74879. https://doi.org/10.18632/oncotarget.20423 (2017).
13. Gatenby, R. A., Grove, O. & Gillies, R. J. Quantitative imaging in cancer evolution and ecology. *Radiology* **269**, 8–15. https://doi.org/10.1148/radiol.13122697 (2013).
14. Swanton, C. Intratumor heterogeneity: evolution through space and time. *Cancer Res.* **72**, 4875–4882. https://doi.org/10.1158/0008-5472.CAN-12-2217 (2012).
15. Chang, Y. C. et al. Delineation of tumor habitats based on dynamic contrast enhanced MRI. *Sci. Rep.* **7**, 9746. https://doi.org/10.1038/s41598-017-09932-5 (2017).
16. Wu, J. et al. Intratumoral Spatial heterogeneity at perfusion MR imaging predicts Recurrence-free survival in locally advanced breast Cancer treated with neoadjuvant chemotherapy. *Radiology* **288**, 26–35. https://doi.org/10.1148/radiol.2018172462 (2018).
17. Kim, M. et al. Spatiotemporal habitats from multiparametric physiologic MRI distinguish tumor progression from treatment-related change in post-treatment glioblastoma. *Eur. Radiol.* **31**, 6374–6383. https://doi.org/10.1007/s00330-021-07718-y (2021).
18. Juan-Albarracin, J. et al. Glioblastoma: vascular habitats detected at preoperative dynamic Susceptibility-weighted Contrast-enhanced perfusion MR imaging predict survival. *Radiology* **287**, 944–954. https://doi.org/10.1148/radiol.2017170845 (2018).
19. Park, J. E. et al. Spatiotemporal heterogeneity in multiparametric physiologic MRI is associated with patient outcomes in IDH-Wildtype glioblastoma. *Clin. Cancer Res.* **27**, 237–245. https://doi.org/10.1158/1078-0432.CCR-20-2156 (2021).
20. Wang, Z. et al. Radiomics and deep learning in nasopharyngeal carcinoma: A review. *IEEE Rev. Biomed. Eng.* **17**, 118–135. https://doi.org/10.1109/RBME.2023.3269776 (2024).
21. Wong, L. M. et al. Convolutional neural network for discriminating nasopharyngeal carcinoma and benign hyperplasia on MRI. *Eur. Radiol.* **31**, 3856–3863. https://doi.org/10.1007/s00330-020-07451-y (2021).
22. Tomita, H. et al. Unenhanced CT texture analysis with machine learning for differentiating between nasopharyngeal cancer and nasopharyngeal malignant lymphoma. *Nagoya J. Med. Sci.* **83**, 135–149. https://doi.org/10.18999/nagjms.83.1.135 (2021).
23. Feng, Q. et al. Radiomics analysis and correlation with metabolic parameters in nasopharyngeal carcinoma based on PET/MR imaging. *Front. Oncol.* **10**, 1619. https://doi.org/10.3389/fonc.2020.01619 (2020).
24. Xu, H., Liu, J., Huang, Y., Zhou, P. & Ren, J. MRI-based radiomics as response predictor to radiochemotherapy for metastatic cervical lymph node in nasopharyngeal carcinoma. *Br. J. Radiol.* **94**, 20201212. https://doi.org/10.1259/bjr.20201212 (2021).
25. Yongfeng, P. et al. The usefulness of pretreatment MR-Based radiomics on early response of neoadjuvant chemotherapy in patients with locally advanced nasopharyngeal carcinoma. *Oncol. Res.* **28**, 605–613. https://doi.org/10.3727/096504020X16022401878096 (2021).
26. Wang, J. et al. A predictive model of radiation-related fibrosis based on the radiomic features of magnetic resonance imaging and computed tomography. *Transl Cancer Res.* **9**, 4726–4738. https://doi.org/10.21037/tcr-20-751 (2020).
27. Liu, Y. et al. Early prediction of acute Xerostomia during radiation therapy for nasopharyngeal cancer based on delta radiomics from CT images. *Quant. Imaging Med. Surg.* **9**, 1288–1302. https://doi.org/10.21037/qims.2019.07.08 (2019).
28. Bao, D. et al. Prognostic and predictive value of radiomics features at MRI in nasopharyngeal carcinoma. *Discov Oncol.* **12**, 63. https://doi.org/10.1007/s12672-021-00460-3 (2021).

29. Li, H. J. et al. Establishment and validation of a novel MRI radiomics Feature-Based prognostic model to predict distant metastasis in endemic nasopharyngeal carcinoma. *Front. Oncol.* **12**, 794975. https://doi.org/10.3389/fonc.2022.794975 (2022).
30. Fan, Y. et al. Subregional radiomics analysis for the detection of the EGFR mutation on thoracic spinal metastases from lung cancer. *Phys. Med. Biol.* **66** https://doi.org/10.1088/1361-6560/ac2ea7 (2021).
31. Cai, Z. et al. Multiparametric MRI subregion radiomics for preoperative assessment of high-risk subregions in microsatellite instability of rectal cancer patients: a multicenter study. *Int. J. Surg.* **110**, 4310–4319. https://doi.org/10.1097/JS9.0000000000001335 (2024).
32. Barker, H. E., Paget, J. T., Khan, A. A. & Harrington, K. J. The tumour microenvironment after radiotherapy: mechanisms of resistance and recurrence. *Nat. Rev. Cancer*. **15**, 409–425. https://doi.org/10.1038/nrc3958 (2015).
33. O'Connor, J. P. et al. Imaging biomarker roadmap for cancer studies. *Nat. Rev. Clin. Oncol.* **14**, 169–186. https://doi.org/10.1038/nrclinonc.2016.162 (2017).
34. Parmar, C. et al. Radiomic feature clusters and prognostic signatures specific for lung and head & neck cancer. *Sci. Rep.* **5**, 11044. https://doi.org/10.1038/srep11044 (2015).
35. Lambin, P. et al. Radiomics: the Bridge between medical imaging and personalized medicine. *Nat. Rev. Clin. Oncol.* **14**, 749–762. https://doi.org/10.1038/nrclinonc.2017.141 (2017).
36. Rao, A., Barkley, D., Franca, G. S. & Yanai, I. Exploring tissue architecture using Spatial transcriptomics. *Nature* **596**, 211–220. https://doi.org/10.1038/s41586-021-03634-9 (2021).
37. Moffitt, J. R. et al. Molecular, Spatial, and functional single-cell profiling of the hypothalamic preoptic region. *Science* **362** https://doi.org/10.1126/science.aau5324 (2018).
38. Vickovic, S. et al. High-definition Spatial transcriptomics for in situ tissue profiling. *Nat. Methods*. **16**, 987–990. https://doi.org/10.1038/s41592-019-0548-y (2019).
39. Shi, Z. et al. MRI-based quantification of intratumoral heterogeneity for predicting treatment response to neoadjuvant chemotherapy in breast Cancer. *Radiology* **308**, e222830. https://doi.org/10.1148/radiol.222830 (2023).
40. van Griethuysen, J. J. M. et al. Computational radiomics system to Decode the radiographic phenotype. *Cancer Res.* **77**, e104–e107. https://doi.org/10.1158/0008-5472.CAN-17-0339 (2017).
41. Zwanenburg, A. et al. The image biomarker standardization initiative: standardized quantitative radiomics for High-Throughput image-based phenotyping. *Radiology* **295**, 328–338. https://doi.org/10.1148/radiol.2020191145 (2020).
42. Natrajan, R. et al. Microenvironmental heterogeneity parallels breast Cancer progression: A Histology-Genomic integration analysis. *PLoS Med.* **13**, e1001961. https://doi.org/10.1371/journal.pmed.1001961 (2016).

Acknowledgements

We thank all the individuals who provided technology support during the research, and all patients and their families involved in the study.

Author contributions

QW and WX were the guarantors of integrity of the entire study. QW was responsible for study concepts and design. QW, WQ and TC carried out the literature research. QW, WQ, QL, YG and KQ carried out the clinical studies. QW and LP were responsible for the experimental studies/data analysis. QW carried out the statistical analysis. QW and WQ prepared the manuscript. QW, WQ and WX edited the manuscript.

Declarations

Competing interests

The authors declare no competing interests.

Ethics approval

This retrospective study was approved by the Ethics Committee of Changzhou First People's Hospital, which waived the need for informed consent from individual patients.

Additional information

Supplementary Information The online version contains supplementary material available at https://doi.org/10.1038/s41598-025-00186-0.

Correspondence and requests for materials should be addressed to W.X.